CHEMISTRY OF MATERIALS

pubs.acs.org/cm

Article

Open Access

This article is licensed under CC-BY-NC-ND 4.0

Diffusion-Limited Solid-State Synthesis Selectivity in the Presence of Oxidation/Reduction Processes

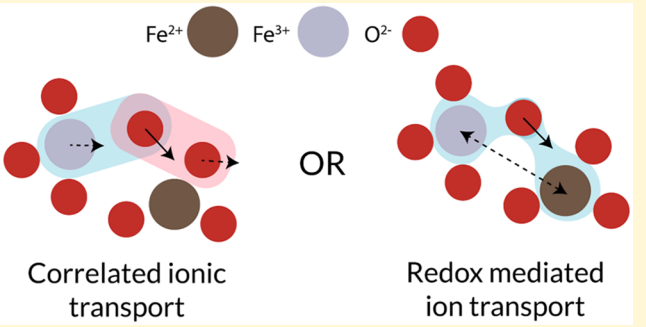
Vir Karan and Kristin A. Persson*

Cite This: *Chem. Mater.* 2026, 38, 10644−10656

Read Online

ACCESS | Metrics & More | Article Recommendations | Supporting Information

ABSTRACT: Solid-state synthesis outcomes arise from an interplay between thermodynamics and kinetics, with their relative importance governed by external control parameters such as temperature profiles and precursor selection. A recently introduced framework, combining first-principles thermodynamics with machine-learning-enabled simulations of correlated ion transport, successfully captured this interplay in the Ba−Ti−O system by linking phase selectivity to ion mobility within "liquid-like", amorphous interphases. Notably, in systems where valence states can change during synthesis, ion dynamics are strongly coupled to oxidation state. Here, we extend the framework to such mixed-valence systems and demonstrate its predictive power for the synthesis of ternary metal ferrites in the Ba−Fe−O and Y−Fe−O systems, benchmarked against in situ XRD experiments. Similar to the Ba−Ti−O system, we hypothesize that the rate-limiting transport of ionic species governing polymorph growth occurs through a "liquid-like," noncrystalline interphase. To capture this behavior, we employ a charge-informed machine-learning potential (CHGNet) that enables modeling of correlated, redox-dependent transport. We find that the framework accurately predicts the sequence of phase formation and the time evolution of phase distributions in powder synthesis reactions, in agreement with experimental reports. These results show that diffusion-limited phase selectivity can be treated on a unified footing across mixed-valence oxides, further clearing a pathway toward rational, in silico synthesis design that simultaneously accounts for thermodynamic and kinetic factors.

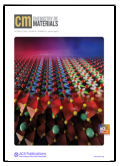


INTRODUCTION

Data-driven design of novel and optimized materials has expanded rapidly over the past decade, placing increasing pressure on synthesis and characterization to realize, or rule out, predicted candidates. Solid-state synthesis remains one of the most technologically important synthesis routes for inorganic materials; however, unlike many material properties, it lacks a general mechanistic and predictive framework. With the advent of large materials databases, first-principles thermodynamic data have been increasingly used to guide synthesis,[1,2] alongside rapid iteration of synthesis recipes enabled by automated laboratories.[3] A significant advance was the pairwise reaction model introduced by Miura et al.,[4] which underpins a suite of subsequent frameworks[1,2,5−7] that incorporate first-principles convex hull energetics to analyze and optimize solid-state powder reactions. Within this context, the "ΔG_{max} hypothesis" selects pathways that minimize the largest free-energy step along a pairwise sequence. More recently, Szymanski et al.[8] critically assessed this hypothesis and identified a practical lower bound of 60 meV/atom in energy differences between competing oxide phases, above which thermodynamic driving forces can reliably predict the operative reaction pathway. While useful, the aforementioned frameworks do not consider the kinetics of these reactions, which can play a decisive role in product phase selectivity. At lower temperatures and/or when thermodynamic driving forces are insufficiently strong or selective, kinetic effects—including diffusion limitations, nucleation barriers, and interfacial processes—become dominant and can significantly alter product selectivity patterns.[9,10] Unlike thermodynamic data, equivalent approaches to incorporate these kinetic effects are not yet supported by large, first-principles databases such as the Materials Project,[11] which hinders a general understanding of the mechanisms at play.

Recently, we introduced an atomistic framework[12] to account for the kinetic effects in solid state synthesis when product selectivity is diffusion-limited in nature. In this approach, the ease of transport of constituent ions across a "liquid-like" or noncrystalline interface between the precursors is computed, which provides information about relative diffusion rates to form different product compositions. We hypothesized that candidate

Received: June 17, 2026
Revised: September 20, 2026
Accepted: September 22, 2026
Published: October 9, 2026



ACS Publications

© 2026 The Authors. Published by American Chemical Society

Downloaded from pubs.acs.org/cmatex/article-pdf/38/20/10644/6879577/acs.chemmater.6c01610.pdf by LAWRENCE BERKELEY NATL LABORATORY user on 06 November 2026

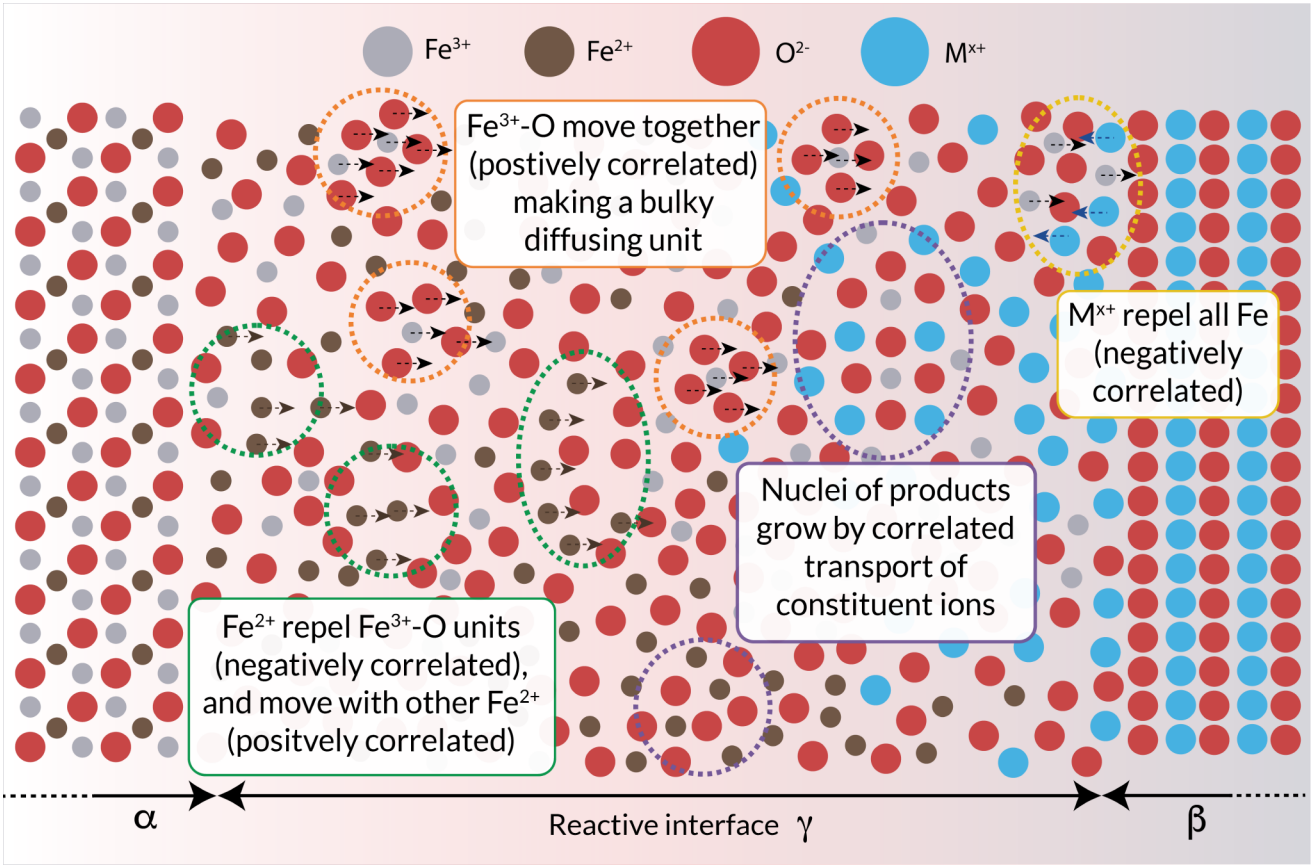


Figure 1. Schematic of the reaction interface (γ) between two powder precursors, α (Fe-rich) and β (M-rich, M = Ba/Y). The nature of ion transport is highly dependent on local coordination environments, which lead to both correlated (positive correlation) and anticorrelated (negative correlation) motion between ions. Compositions of the interface (γ) that allow for rapid transport support faster growth of product nuclei, and hence influence product selectivity during the reaction.

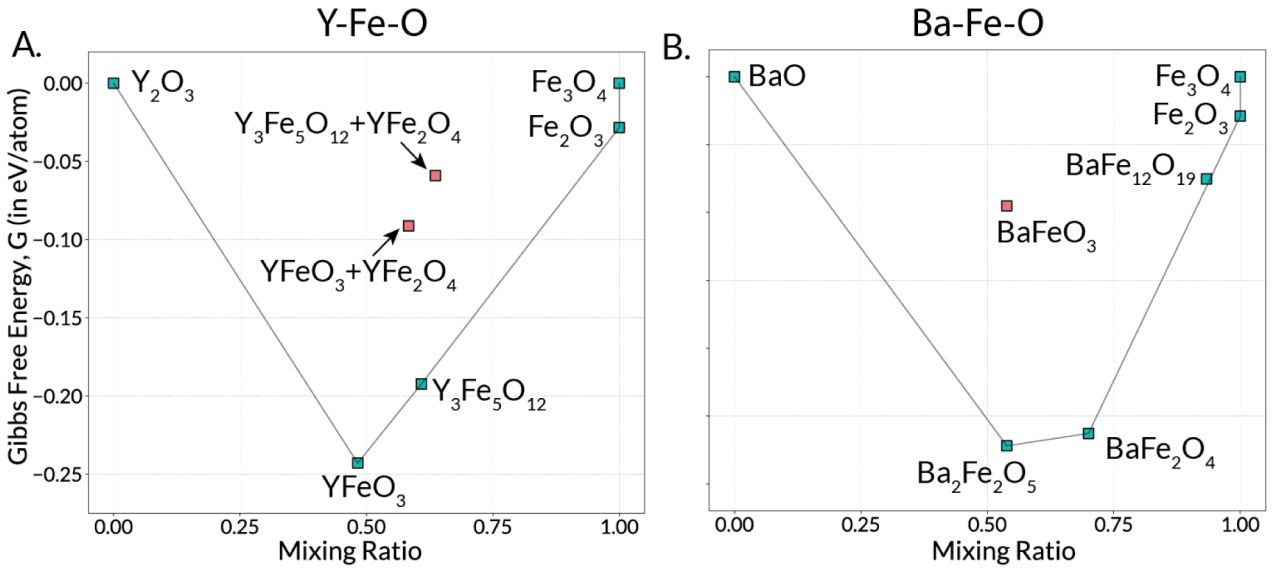


Figure 2. Thermodynamic hulls of stability at 800 °C and atmospheric pressure computed between: A) Y_2O_3 and Fe_3O_4; and B.) BaO and Fe_3O_4. The corresponding convex hulls including Fe_2O_3 as a reactant are also shown in the same figure, with only experimentally observed phases displayed. The red squares represent metastable phases under atmospheric pressure.

nucleating phases fail to grow when the compositionally equivalent liquid-like interphase exhibits sluggish diffusion, providing a physically motivated descriptor for diffusion-limited selectivity (Figure 1). This framework rationalized experimentally observed synthesis outcomes in the Ba−Ti−O chemical space that deviate from predictions based solely on the thermodynamic convex hull, and, when coupled with simulations of phase evolution using a cellular-automaton framework

https://doi.org/10.1021/acs.chemmater.6c01610
Chem. Mater. 2026, 38, 10644−10656

Downloaded from pubs.acs.org/cmatex/article-pdf/38/20/10644/6879577/acs.chemmater.6c01610.pdf by LAWRENCE BERKELEY NATL LABORATORY user on 06 November 2026

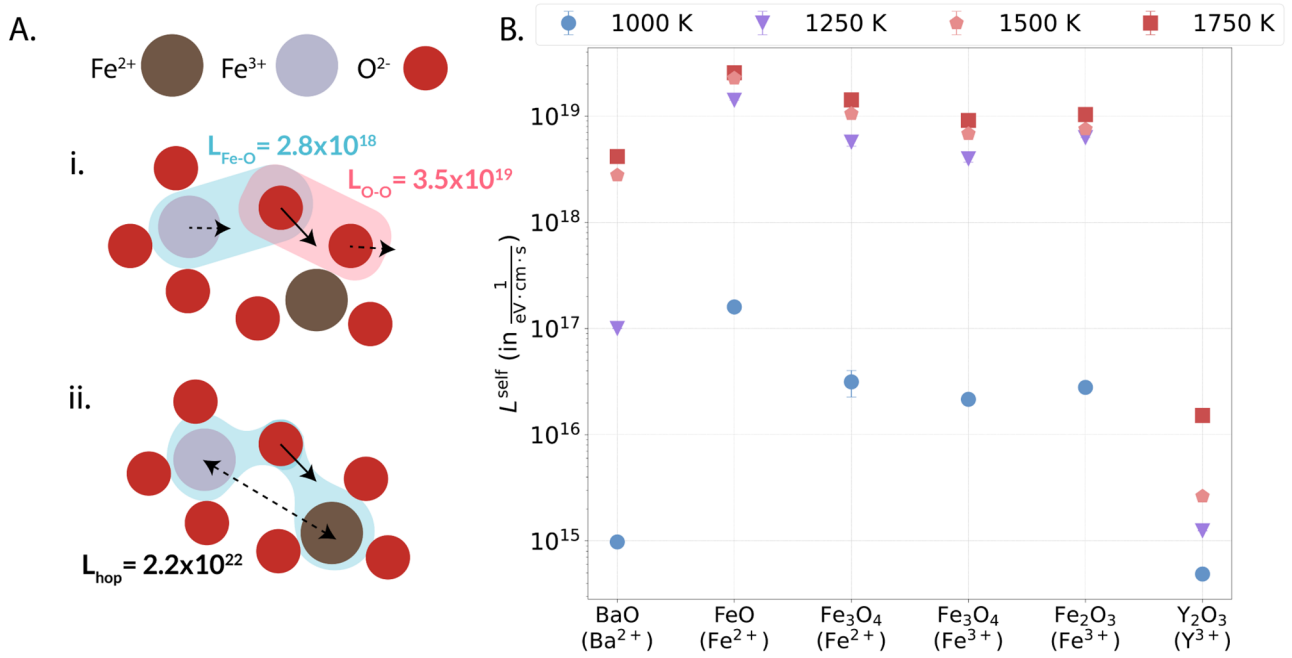


Figure 3. A: Schematic of the available relaxation mechanisms of an amorphous system to a perturbation: (i) displacement of an O^{2-} induces a movement in the nearest ions (an Fe^{3+} and another O^{2-}), leading to correlated ionic motion while retaining the nature of bonding between these ions; (ii) the same displacement instead changes the bonding, i.e., the extent of charge transfer between the Fe^{3+}-O^{2-} and the nearby Fe^{2+}–O^{2-}. In the extreme case, this leads to a coupled reduction of Fe^{3+} and oxidation of Fe^{2+}, i.e., a Fe^{2+}/Fe^{3+} redox reaction or a polaron hop. The magnitude of the computed kinetic coefficients (L) are shown for Fe_3O_4 at 1500K, in units of $1/(eV{\cdot}cm{\cdot}sec)$. Since polaron hopping occurs on a time scale much faster than ionic motion, such that charge redistribution effectively equilibrates instantaneously for a given ionic configuration, it allows redox states to be treated as adiabatically adjusted to the local atomic environment. B: Transport self-coefficients of the metal ion in various binary oxides in their noncrystalline states. We note that transport of Fe in its oxides is faster than that of Ba or Y in their respective oxides, and that within Fe_3O_4, Fe^{2+} exhibits higher mobility than Fe^{3+}.

(ReactCA),[6] showed excellent agreement with prior experimental studies of this system.

While the present approach demonstrates encouraging success in capturing the challenging polymorphism of the Ba–Ti–O system, this system—despite its highly competitive energetics—retains fixed ionic valence states during synthesis, a condition that does not generally hold for most solid-state reactions. Extending the framework to more general synthesis conditions requires explicitly accounting for species capable of adopting multiple oxidation states and undergoing charge transfer during diffusion, recognizing that redox activity can strongly influence ion transport and reaction kinetics.[13−16] This complexity is particularly pronounced for transition-metal-containing systems, where readily available binary precursors span a wide range of oxidation states. The presence of such species not only enables redox-active transport but also increases the tolerance for off-stoichiometry and promotes the formation of solid solutions. Consequently, precursor selection becomes nontrivial, as both thermodynamic driving forces and transport properties depend on the evolving oxidation states of the transition metals under reaction conditions.

Here we extend our mechanistic framework to account for the effect of changing oxidation state on correlated ionic transport through reactive interphases, and showcase its application to the solid-state synthesis of metal ferrites, M–Fe-O (M = Ba/Y). These systems are chosen since the phases with the transition metal in a mixed oxidation state can reasonably be approximated as line-compounds. This distinction allows us to isolate the effect of valence state on transport by removing the complexity associated with modeling charged defect–defect interactions that can lead to significantly different thermodynamic driving forces.[17−19] Furthermore, as is apparent from the thermodynamic stability hulls (Figure 2), the differences in the thermodynamic driving force to form various Y/Ba–Fe–O phases are often small (≤100 meV/atom), which manifests as strong phase competition during a solid-state synthesis reaction performed at elevated temperatures. Due to such small energy differences, product selectivity often becomes limited by reaction kinetics.[8] Recently, Chen et al.[20] employed the reaction network approach of McDermott et al.[5] to study synthesis reactions in the Y/Ba–Fe–O chemical space, based on thermodynamic data from the Materials Project at the GGA level of theory alone. Indeed, Chen et al. correctly identified $YFeO_3$ as the first phase to form in the reaction between Y_2O_3 and Fe_2O_3, consistent with the convex hull (Figure 2), however, in contrast, for the Ba–Fe–O system, experiments show that $BaFe_{12}O_{19}$ forms first, a result that is not captured by the thermodynamic model.

It is worth noting that, in a few solid-state reactions, the magnetic ordering and structural framework of the precursors can influence the selectivity of the first product phase, effectively lowering the nucleation barrier for structurally or magnetically compatible products.[21] However, in the synthesis of these metal ferrites, both the precursor framework and magnetic ordering are not preserved. Instead, phases that persist as impurities during synthesis often exhibit a propensity to form superlattices,[22,23] indicating a distinct selection mechanism that is not governed by structural inheritance.

To assess whether the mechanistic framework of Karan et al.[12] can be extended to ferrite systems, we fine-tune the charge-

Downloaded from pubs.acs.org/cmatex/article-pdf/38/20/10644/6879577/acs.chemmater.6c01610.pdf by LAWRENCE BERKELEY NATL LABORATORY user on 06 November 2026

https://doi.org/10.1021/acs.chemmater.6c01610
Chem. Mater. 2026, 38, 10644−10656

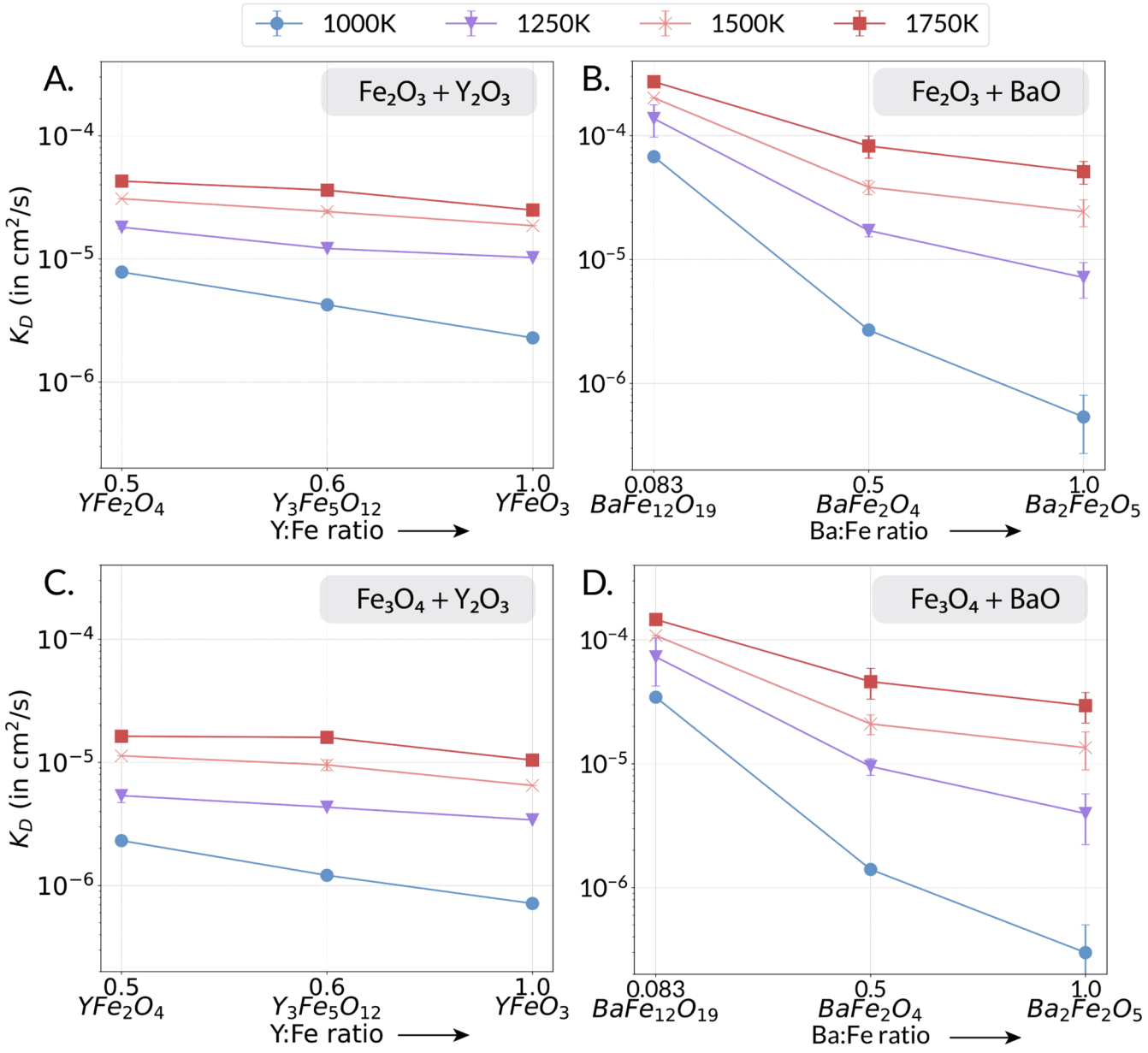


Figure 4. Effective diffusional rate constants (K_D) across liquid-like products of compositions ordered by decreasing Fe content for A) $Fe_2O_3 + Y_2O_3$ as reactants; B) Fe_2O_3 + BaO as reactants; C) $Fe_3O_4 + Y_2O_3$ as reactants; and D) Fe_3O_4 + BaO as reactants.

aware, machine-learned interatomic potential (MLIP) CHGNet[24,25] using high-quality DFT data for liquid-like, noncrystalline phases computed at the r^{2}SCAN level of theory. Within the framework, the growth-limiting transport is described through amorphous analogs of the relevant phases, explicitly capturing the influence of nominal oxidation states on ionic interactions. We quantify transport across reaction interfaces using an effective diffusion rate constant, K_D,[12] evaluated for noncrystalline representations of the expected product phases. These results are subsequently integrated into powder reaction simulations using a cellular automaton approach (ReactCA).[6] We examine the effect of precursor choice (Fe_2O_3 vs Fe_3O_4) on phase evolution during synthesis reactions targeting well-studied technologically relevant ternary metal ferrite phases such as the $BaFe_{12}O_{19}$ hexaferrite, the $BaFe_2O_4$ spinel, the $Y_3Fe_5O_{12}$ garnet and the $BaFeO_{3-x}$ perovskite.[26,27] Comparison with existing synthesis literature demonstrates that the framework accurately predicts both the identity of the first phases to form and the evolving phase distribution throughout the reaction. Our results confirm that the mechanistic framework of Karan et al.[12]—which models solid-state synthesis from an atomistic perspective by coupling a first-principles, thermodynamics-based reaction network with diffusion limitations mediated through an amorphous reaction interphase—provides a robust and predictive description of phase evolution, extending to systems with redox-active transition metal ions.

RESULTS AND DISCUSSION

Adiabatic Treatment of Redox Reactions and Ionic Transport

In order to treat ionic diffusion and redox processes adiabatically, we first ensure that the two processes can be robustly decoupled for the purposes of the transport simulation. We

Downloaded from pubs.acs.org/cmatex/article-pdf/38/20/10644/6879577/acs.chemmater.6c01610.pdf by LAWRENCE BERKELEY NATL LABORATORY user on 06 November 2026

https://doi.org/10.1021/acs.chemmater.6c01610
Chem. Mater. 2026, 38, 10644−10656

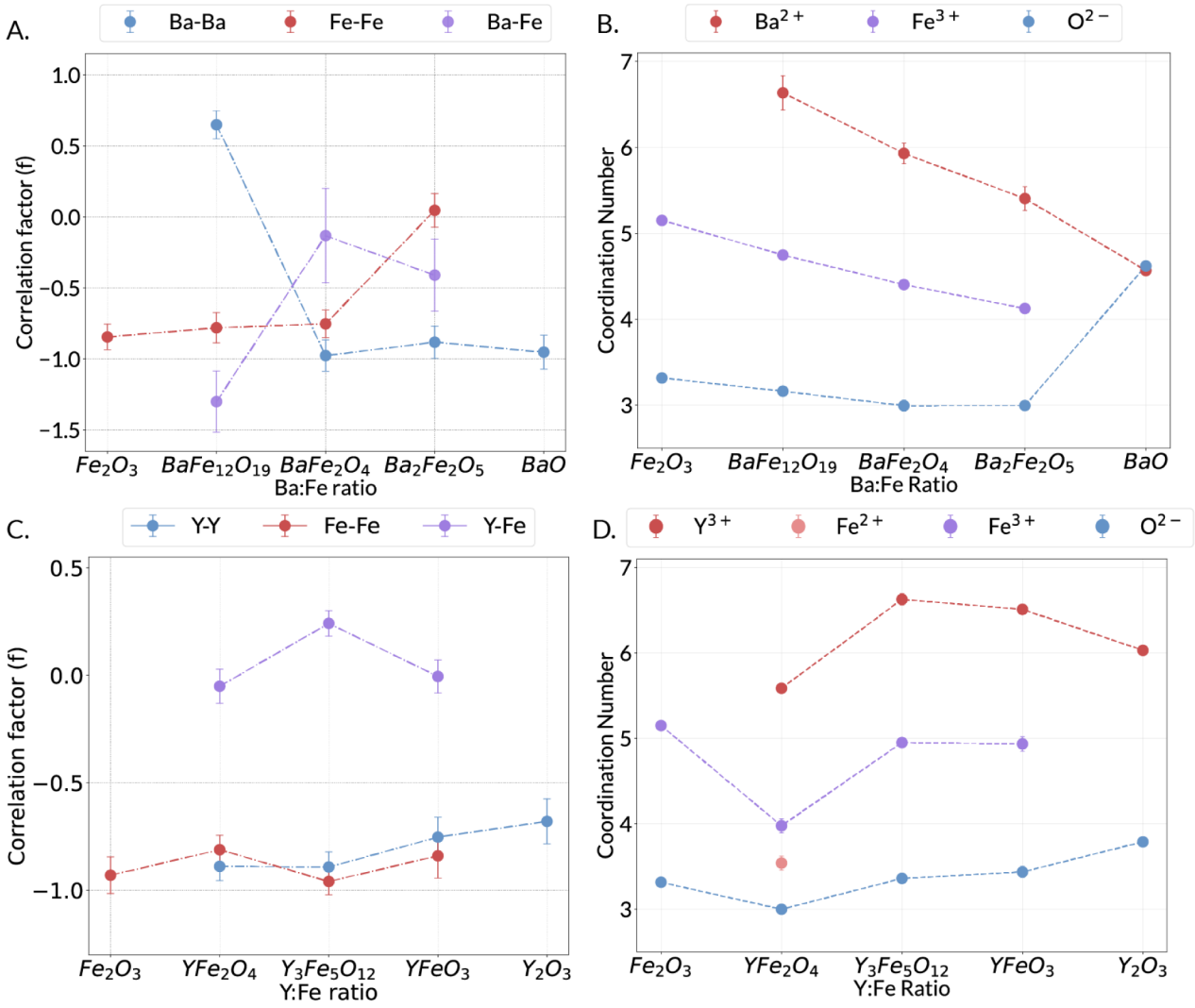


Figure 5. A, C: Correlation factor for different cation-pairs in Ba−Fe−O and Y−Fe−O phases respectively; B, D: Coordination number of ions in Ba−Fe−O and Y−Fe−O phases respectively, considering neighbor lists up to the second coordination shell.

consider the two classical limits of the dynamic response of a noncrystalline system to a perturbation (ionic displacement) that induces a local electric field.[28] In the first limit, the induced field is relaxed primarily through correlated ionic motion (as in Karan et al.;[12] see Figure 3Ai). In the second limit, the induced field is relaxed primarily through electronic charge transfer (redox) between mixed-valence sites, e.g., a small-polaron hop,[29,30] see Figure 3Aii. Physically, these scenarios correspond to the two limits of the screening length (λ) of the induced field. A derivation of this screening length at the continuum scale considering these two limits of screening is provided in the (Supporting Information SI). We note that quantum-mechanical kinetic effects, such as the ligand-exchange inertness of specific spin configurations (e.g., low-spin Co^{3+}/Ir^{3+}),[31] lie beyond the classical, adiabatic treatment adopted here, though their influence is expected to be limited at the elevated temperatures and in the disordered interphases consider here.

From MLIP-MD simulations of mixed-valence, noncrystalline oxides (see SI), we find that the relevant transport behavior is well described by the strong-screening limit, i.e., the $\lambda \to 0$ regime, where fields induced due to thermal, ionic displacements are efficiently screened by rapid charge transfer. This is consistent with prior literature,[30,32,33] which shows that polaronic hopping in such oxides is orders of magnitude faster than ionic motion (see Figure 3A). Hence, in the mixed-valence oxides considered here, we assume that redox exchange between neighboring Fe ions can be treated as effectively instantaneous. Ionic transport is therefore modeled by treating Fe^{2+} and Fe^{3+} as distinct species with separately fitted transport coefficients, classified via site-resolved magnetic moments under overall charge neutrality. This assignment reflects local coordination environments and should be interpreted as relative rather than a strict mapping to formal charge states.[16]

While Fe^{2+} and Fe^{3+} are treated as distinct species, the growth rate of a product nucleus in a solid-state reaction is governed by the mass transport of Fe of any valence; accordingly, their contributions to transport are additive in the evaluation of K_D. This treatment allows the previous framework[12] to be extended to systems with redox-active ions by decomposing them into their constituent species, provided that screening via polaronic motion is effectively instantaneous, as compared to ionic motion. The numerical validation and physical constraints underlying this approximation are detailed in the Methods and SI.

Downloaded from pubs.acs.org/cmatex/article-pdf/38/20/10644/6879577/acs.chemmater.6c01610.pdf by LAWRENCE BERKELEY NATL LABORATORY user on 06 November 2026

https://doi.org/10.1021/acs.chemmater.6c01610
Chem. Mater. 2026, 38, 10644−10656

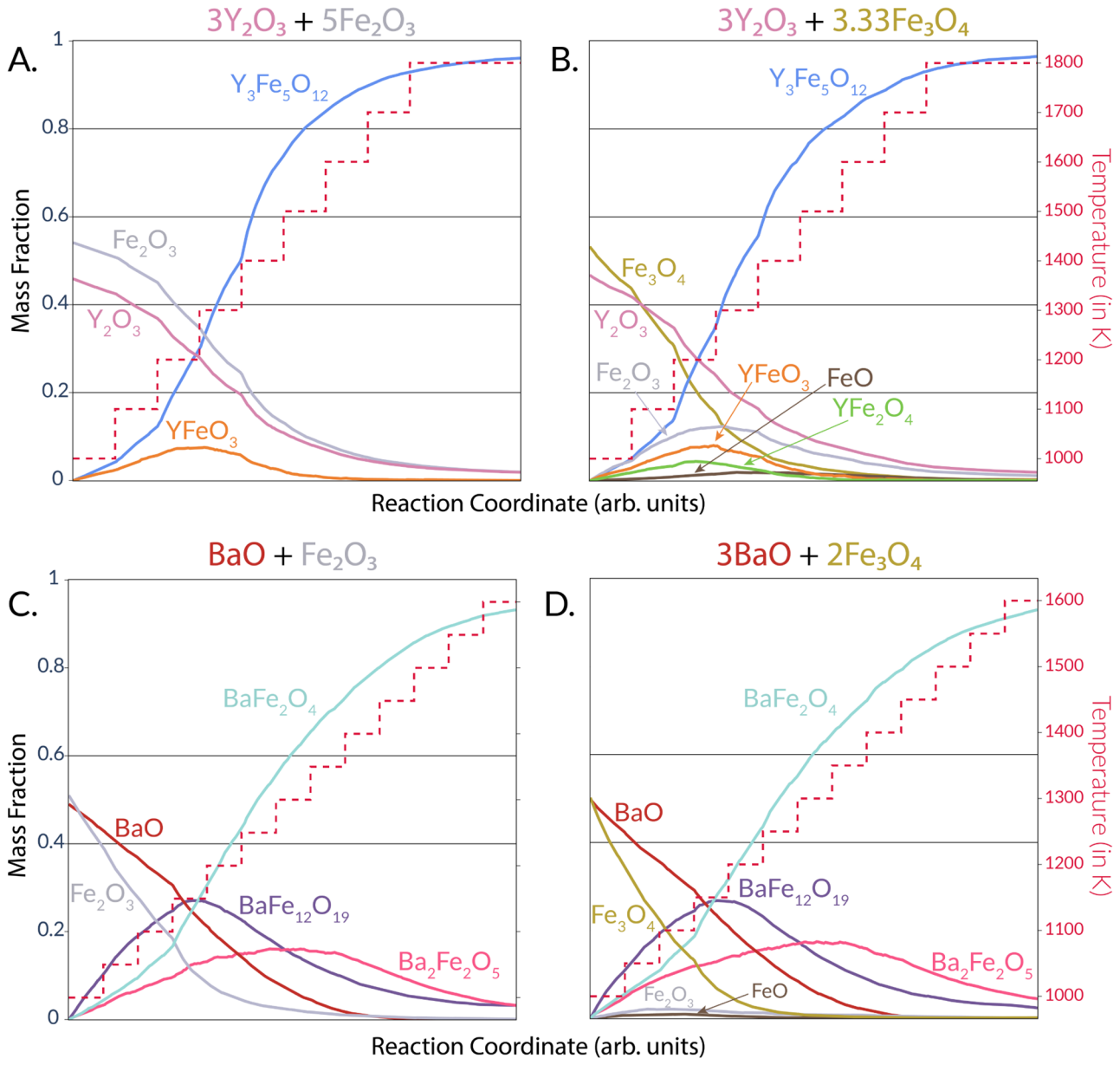


Figure 6. ReactCA simulations of powder synthesis reactions of A) $3Y_2O_3 + 5Fe_2O_3$ (3:5 ratio of Y:Fe); B) $3Y_2O_3 + 3.33Fe_3O_4$ (3:5 ratio of Y:Fe); C) $BaO + Fe_2O_3$ (1:2 ratio of Ba:Fe); and D) $3BaO + 2Fe_3O_4$ (1:2 ratio of Ba:Fe). All simulations are performed under a fixed oxygen chemical potential corresponding to $p_{O_2} = 0.21$atm (air).

Transport through Liquid-Like, Noncrystalline Interphases

Figure 3B shows the computed transport coefficients of metal ions in noncrystalline analogues of the precursors as a function of temperature. Fe exhibits systematically higher mobility than Ba and Y, with Fe^{2+} diffusing faster than Fe^{3+}. Analysis of Fe−Fe correlations suggests that this behavior arises from weaker (less negative) interactions in the lower oxidation state, matching prior reports of transport in molten $Fe_{1-x}O$ oxides with mixed Fe^{2+}/Fe^{3+}.[34] This trend is consistent with the relative melting points of the corresponding oxides, which decrease in the order $Y_2O_3 > BaO > Fe_2O_3 \approx Fe_3O_4 > FeO$.[35] We provide a detailed comparison of our computed self-diffusion data to existing experimentally measured transport data in the (Supporting Information SI).

On the other hand, the effective diffusion rate constants, K_D (defined in eq 2 of the Methods) across the Y−Fe−O and Ba−Fe−O phases are shown in Figure 4. We observe a clear contrast between the two systems: the variation in K_D across the Ba−Fe−O system is far more pronounced, spanning several orders of magnitude at each temperature, whereas in Y−Fe−O it varies by less than half an order of magnitude. In the Ba−Fe−O system, $BaFe_{12}O_{19}$ exhibits a distinct kinetic advantage over competing phases, which are thermodynamic sinks, resulting in a strong interplay between kinetics and thermodynamics in phase selection. In contrast, in the Y−Fe−O system, noncrystalline Y−Fe−O with composition YFe_2O_4 shows only a modest kinetic enhancement (≈2× faster) at ≥100 meV/atom above the convex hull, substantially limiting its competitiveness for growth under typical solid-state synthesis conditions. This trend also aligns with the parabolic rate constants (k_p) fitted by Buscaglia et al.[36] for $YFeO_3$ and $Y_3Fe_5O_{12}$ reaction-diffusion couples, in particular recovering the modestly faster growth rate of

https://doi.org/10.1021/acs.chemmater.6c01610
Chem. Mater. 2026, 38, 10644−10656

Downloaded from pubs.acs.org/cmatex/article-pdf/38/20/10644/6879577/acs.chemmater.6c01610.pdf by LAWRENCE BERKELEY NATL LABORATORY user on 06 November 2026

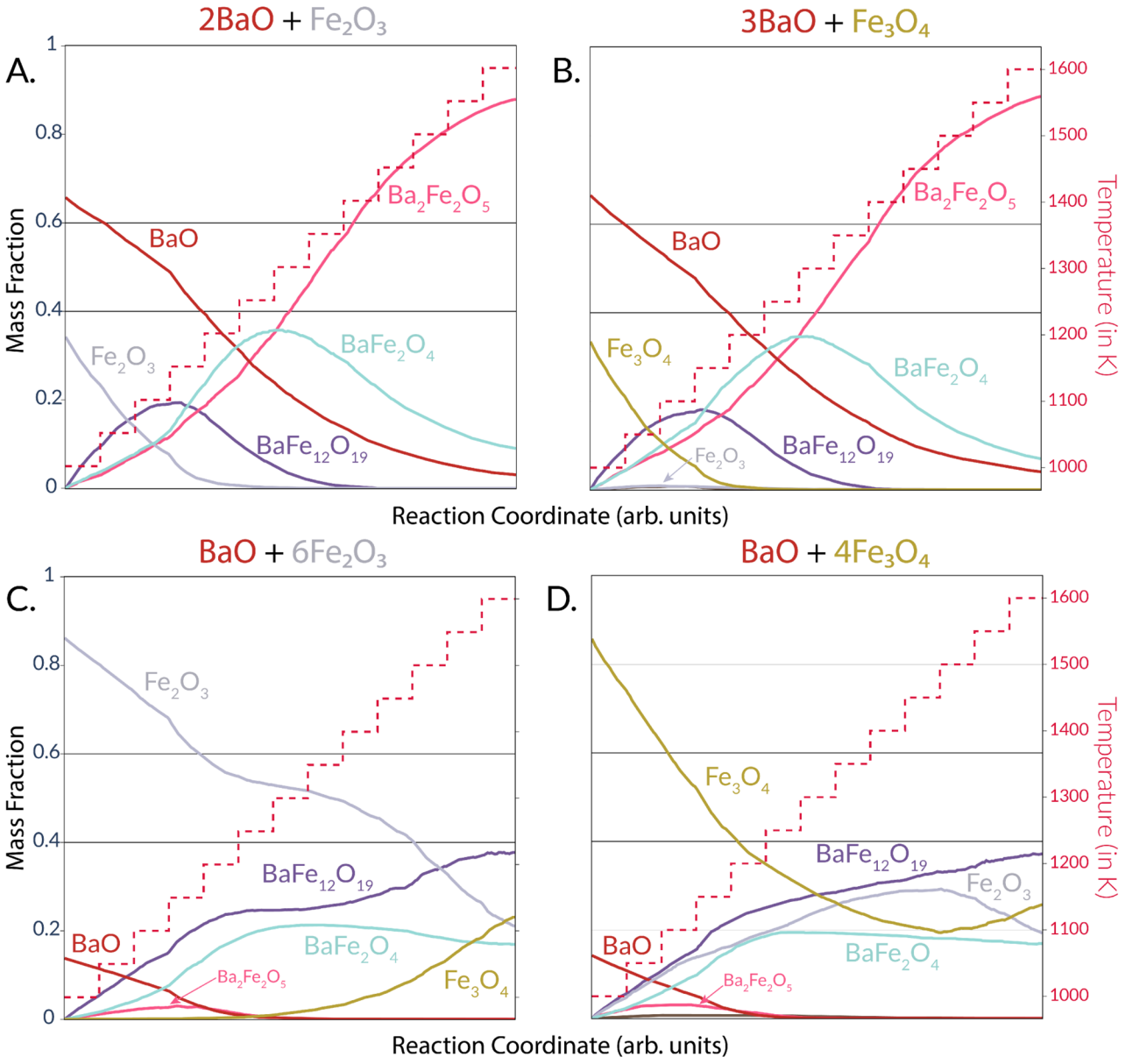


Figure 7. ReactCA simulations of powder synthesis reactions of A) $2BaO + Fe_2O_3$ (1:1 ratio of Ba:Fe); B) $3BaO + Fe_3O_4$ (1:1 ratio of Ba:Fe); C) $BaO + 6Fe_2O_3$ (1:12 ratio of Ba:Fe); and D) $BaO + 4Fe_3O_4$ (1:12 ratio of Ba:Fe). All simulations are performed under a fixed oxygen chemical potential corresponding to $p_{O_2} = 0.21$atm (air).

$Y_3Fe_5O_{12}$ over $YFeO_3$ at the temperatures we consider in this study.

To rationalize these trends, we analyzed both the local coordination environments of each product phase and the corresponding ion−ion correlations—specifically Ba−Ba, Fe−Fe, Y−Y, Ba−Fe, and Y−Fe—as shown in Figure 5A. These correlations are quantified by the correlation factor (f_i), $f_i = \frac{L_{ii}^{dis}}{L_{ii}^{self}}$, which measures deviations from dilute-limit transport arising from collective ionic motion. We find that O^{2-} is consistently positively correlated with Fe^{3+} and negatively correlated with Ba^{2+}, while its correlations with Fe^{2+} and Y^{3+} vary in sign. This behavior agrees with the expected coordination chemistry based on bond lengths, indicating the presence of highly coordinated Fe^{3+}−O clusters that are interconnected by Ba, Y, or lower-coordinated Fe^{2+}. These observations are consistent with prior studies of transport in liquid-like Ba−Ti−O intermediates.[12]

Furthermore, in the Ba−Fe−O system, two distinct diffusion regimes emerge. At low Ba content, where Ba−Ba interactions are effectively screened by the surrounding ionic environment, Ba ions exhibit cooperative motion, as indicated by a positive Ba−Ba correlation factor, while Ba−Fe and Fe−Fe correlations remain negative, consistent with cation−cation repulsion. In contrast, at high Ba content, this behavior is largely inverted: Ba−Ba correlations become strongly negative, Ba−Fe correlations remain moderately negative, and Fe−Fe correlations approach zero. By comparison, the Y−Fe−O system shows no significant change in Y−Fe correlated kinetics with composition, and the transport rates depend only weakly on the Y:Fe ratio. We corroborate this analysis by examining the coordination numbers of different ions: the coordination number of Ba in $BaFe_{12}O_{19}$ is ≈6.9 and decreases with increasing Ba content. The

https://doi.org/10.1021/acs.chemmater.6c01610
Chem. Mater. 2026, 38, 10644−10656

Downloaded from pubs.acs.org/cmatex/article-pdf/38/20/10644/6879577/acs.chemmater.6c01610.pdf by LAWRENCE BERKELEY NATL LABORATORY user on 06 November 2026

Table 1. Comparison of Simulation vs Experimental Reports for Reaction Tested with Fe_2O_3 Precursor[a]

Reaction	Outcome		First phase to form	
	Simulation	Experiment	Simulation	Experiment
$3Y_2O_3 + 5Fe_2O_3$	$Y_3Fe_5O_{12}$	$Y_3Fe_5O_{12}$	$YFeO_3$	$YFeO_3$
$BaO + Fe_2O_3$	$BaFe_2O_4$, $BaFe_{12}O_{19}$, $Ba_2Fe_2O_5$	$BaFe_2O_4$	$BaFe_{12}O_{19}$	$BaFe_{12}O_{19}$
$2BaO + Fe_2O_3$	$Ba_2Fe_2O_5$, $BaFe_2O_4$	$BaFeO_{3-x}$	$BaFe_{12}O_{19}$	$BaFe_{12}O_{19}$
$BaO + 6Fe_2O_3$	$BaFe_{12}O_{19}$, Fe_3O_4, $BaFe_2O_4$, Fe_2O_3	$BaFe_{12}O_{19}$, Fe_3O_4, $BaFe_2O_4$	$BaFe_{12}O_{19}$	$BaFe_{12}O_{19}$, $BaFe_2O_4$

[a]The kinetically informed simulation correctly captures the first phase to form as well as the final product distribution in all cases.

coordination number of Fe also decreases as the Ba content in the phase increases. Considering the coordination structure to be Fe−O clusters bridged with Ba-ions, increasing Ba content leads to an increased repulsion between the Ba−Ba cations, leading to a lower overall coordination.

The differences in local coordination preferences between the Y−Fe−O and Ba−Fe−O phases are primarily driven by ionic size, with Ba^{2+} (1.35 Å) being substantially larger than both Fe^{3+} (0.645 Å) and Y^{3+} (0.9 Å). This larger size disparity in the Ba−Fe system leads to more pronounced variations in transport behavior compared to Y−Fe−O. The larger relative size of Ba here distorts the Fe−O network, leading to a higher degree of Ba−Ba coordination on increasing Ba-content.[37] Consequently, $BaFe_{12}O_{19}$, with its low Ba content, gains a strong kinetic advantage over competing phases, explaining its emergence as the first phase to form during solid-state synthesis.

ReactCA Simulations of Powder Reactions

To understand and probe broad product selectivity in synthesis reactions in the Ba−Fe−O and Y−Fe−O chemical spaces, we simulate powder reactions using a cellular automaton approach. These simulations use both the first-principles thermodynamic data based on the convex hull (Figure 2) and the computed K_D (Figure 4) to propagate reactions based on a predefined scoring function (eq 4 in Methods). We use fixed precursors for Ba^{2+} (BaO) and Y^{3+} (Y_2O_3), and choose from either Fe_2O_3 or Fe_3O_4 as the source for Fe. The global ratio of Ba:Fe or Y:Fe is systematically varied while keeping a fixed heating profile from 1000 K−1600 K over 1000 simulation steps for the Ba−Fe−O system and 1000 K−1800 K over 1000 simulation steps for the Y−Fe−O system, with the aim of uncovering trends in product selectivity as a function of reaction progression and Fe precursor choice. The reactions are performed under atmospheric O_2, with a fixed chemical potential corresponding to $p_{O_2} = 0.21$atm, under the assumption that transport of environmental oxygen is facile and remains in equilibrium with the oxygen content of the precursors.

The evolution of phase mass fractions during the simulations are shown in Figures 6 and 7, with a summary of the results provided in Table 1. All reactions proceed at high temperature toward the most thermodynamically stable phase with the global composition of the system (Figure 2), with minimal (≤20 weight%) impurity phases. However, the first phase to form deviates from thermodynamic expectations, and our approach accurately captures this nonequilibrium sequence of phases observed during the reaction.

In Figure 6A and B, the global composition is set to target $Y_3Fe_5O_{12}$ (Y:Fe = 3:5), and upon heating above 1400 K, the simulations correspondingly evolve toward phase-pure $Y_3Fe_5O_{12}$ as the final product. At lower temperatures, in the beginning of the simulation, a transient $YFeO_3$ impurity is observed for both Fe_2O_3 and Fe_3O_4 precursors, in excellent agreement with experimental reports by Holmquist et al.,[38] Peelamedu et al.,[39] Grosseau et al.,[40] and Ali et al.[41] No additional impurity phases are predicted when using the Fe_2O_3 precursor. In contrast, simulations with Fe_3O_4 as precursor show the formation of various impurities of Fe_2O_3, FeO, and YFe_2O_4, although only Fe_2O_3 exceeds ≈3% abundance. The appearance of these phases is consistent with the oxidation pathway by which Fe^{2+} in Fe_3O_4 converts to Fe^{3+} in $Y_3Fe_5O_{12}$, as previously suggested by Cortes et al.,[42] who proposed Fe^{2+} containing intermediates form due to due to the faster diffusive transport of Fe^{2+} compared to Fe^{3+}. These Fe^{2+} intermediates then oxidize in the presence of atmospheric O_2 to yield the Fe^{3+} target phases. The absence of these intermediates in prior XRD studies (Holmquist et al., Grosseau et al., Ali et al.) likely reflects their low concentrations or noncrystalline character, which renders them difficult to detect with in situ XRD. Notably, we observe that the maximum fraction of $YFeO_3$ impurity increases by ≈1.3% when using Fe_3O_4, consistent with established synthesis principles that enhancing thermodynamic driving forces through precursor selection primarily accelerates the formation of the initial phase(s).[2,43]

In Figure 6C and D, the global composition is set to target $BaFe_2O_4$ (Ba:Fe = 1:2), while Figure 7A and B target $Ba_2Fe_2O_5$ (Ba:Fe = 1:1). For both precursor sets, upon heating above 1200 K, the simulations converge to the intended final phase, with the primary impurities being $Ba_2Fe_2O_5$ + $BaFe_{12}O_{19}$ and $BaFe_2O_4$, respectively. This behavior is expected given the near-degeneracy in the formation energies of $BaFe_2O_4$ and $Ba_2Fe_2O_5$ (Figure 2B). More notably, $BaFe_{12}O_{19}$, while being on the hull, is ≈200 meV/atom less favorable at the given stoichiometric reaction, and consistently appears in all four reactions as an early forming impurity, reflecting its strong kinetic advantage driven by rapid transport.[44−46] As in the Y−Fe−O system, the use of Fe_3O_4 as a precursor also leads to the transient formation of Fe_2O_3 and FeO, providing further evidence for an oxidation pathway of Fe^{2+} mediated by FeO intermediates.

In Figure 7C and D, the global composition targets $BaFe_{12}O_{19}$ (Ba:Fe = 1:12), a phase that proves difficult to obtain in a phase-pure form compared to the previous cases. Instead, we observe persistent impurities of $BaFe_2O_4$, Fe_2O_3, and Fe_3O_4. The relative amounts of Fe_2O_3 and Fe_3O_4 depend strongly on temperature: above ≈1500 K, the reaction $Fe_2O_3 \rightarrow Fe_3O_4 + O_2$ becomes thermodynamically favorable, converting residual Fe_2O_3 into Fe_3O_4. These trends are in excellent agreement with experimental observations—Melzer et al.[44] and Shipko et al.[46] report the presence of $BaFe_2O_4$ in samples annealed between 1250−1500 K and a sharp increase in Fe_3O_4 at 1600 K. Additionally, Melzer et al. observed small amounts of $BaFeO_{3-x}$, which under the present atmospheric O_2 conditions corresponds to $Ba_2Fe_2O_5$.[26,47] In addition, the absence of the Fe(IV) phase ($BaFeO_3$) from our simulations and experiments can be rationalized by its high degree of metastability (≥150 meV/atom above the hull). This phase has been previously

Downloaded from pubs.acs.org/cmatex/article-pdf/38/20/10644/6879577/acs.chemmater.6c01610.pdf by LAWRENCE BERKELEY NATL LABORATORY user on 06 November 2026

https://doi.org/10.1021/acs.chemmater.6c01610
Chem. Mater. 2026, 38, 10644−10656

synthesized with ease in oxygen-rich atmospheres,[47,48] under which conditions this phase appears on the hull.

Compared to the in situ experiments of Chen et al.,[20] which report near-complete conversion to $BaFe_{12}O_{19}$, our simulations underestimate the final phase purity and predict a delayed onset of $BaFe_2O_4$, in agreement with the experiments of Melzer et al.[44] and Shipko et al.[46] A key distinction lies in precursor evolution: in Chen et al., the Ba source ($BaCO_3$) converts almost entirely to $BaFe_2O_4$ prior to significant solid-state reaction (well below 973 K). Such prereaction transformations can be observed under high-energy ball milling conditions[45] which effectively alter the reaction pathway by modifying the initial state of the system. In contrast, under the conditions considered here (1000−1600 K) with BaO as the Ba source, achieving phase-pure $BaFe_{12}O_{19}$ is known to be challenging and often requires excess BaO,[49] as well as intermittent regrinding to regenerate reactive interfaces.

Finally, and in contrast to our work, the thermodynamic reaction network analysis of Chen et al.[20] identified $Ba_2Fe_6O_{11}$ as a potential intermediate in the synthesis of $BaFe_{12}O_{19}$. Although this phase has been reported experimentally, it is highly metastable and has only been observed under specialized conditions, specifically when $BaO-Fe_2O_3$ mixtures are reacted with B_2O_3 to form a glassy intermediate.[50] It has not been detected in conventional powder reactions within the Ba−Fe−O system for several decades, except for the study in ref 50. Furthermore, based on GGA-level thermodynamic data from the Materials Project, Chen et al.[20] suggested that both $BaFe_2O_4$ and $BaFe_{12}O_{19}$ are metastable and appear only due to kinetic stabilization. In contrast, our higher-fidelity r^{2}SCAN calculations, incorporating improved finite-temperature corrections, indicate that both phases appear on the convex hull at temperatures as low as ≈800 °C (1073 K), and are therefore thermodynamically stable under typical synthesis conditions.

In summary, across all Ba−Fe−O reactions, our combined thermodynamic and kinetics-informed simulations accurately reproduce the experimentally observed products and key intermediates, including the kinetically selected $BaFe_{12}O_{19}$ phase. The model also captures experimentally reported trends in the relative phase abundances as a function of the Fe precursor, demonstrating its ability to resolve precursor-dependent reaction pathways.

CONCLUSION

This study provides mechanistic insight into the role of transport kinetics in precursor selection for solid state powder synthesis. In the adiabatic limit, we argue that polaronic hopping is orders of magnitude faster than ionic motion and can be treated as effectively instantaneous, allowing ionic transport to be modeled independently with redox states represented as distinct species. Under this assumption, we show that redox reactions in mixed-valence oxides can be incorporated into the kinetic selectivity framework with minimal modification by treating distinct oxidation states as separate species in the transport model. By comparing phase selection in Y−Fe−O and Ba−Fe−O systems, we reveal a delicate interplay between thermodynamic driving forces and kinetic accessibility, mediated by transport through noncrystalline reaction intermediates. Our simulations quantitatively reproduce the experimentally observed phase evolution and correctly capture the kinetically selected first phases to form. This work extends and further demonstrates the predictive capability of the previously proposed mechanistic reaction automaton, establishing it as a robust, atomistic framework for an in-silico synthesis digital twin.

METHODS

Interatomic Potential Development

An accurate treatment of iron and its oxides using DFT remains particularly challenging, and—at the GGA level of theory—requires the use of a + U correction to retrieve the correct charge localization and hence the correct formation enthalpies.[51] The choice of an appropriate + U however depends on the composition of the iron oxide, and will have to be recomputed for noncrystalline variants of the same composition. Hence, in this study, we use only high-quality DFT data computed at the r^{2}SCAN level of theory, which has been shown to be highly accurate in computing the formation enthalpies and related properties of such oxides.[52]

We build on recent advances in foundation machine-learned interatomic potentials by using the MatPES-trained CHGNet model (`CHGNet-MatPES-r2SCAN-2025.2.10-2.7M-PES`)[24,25] as the starting point for this study. Following the methodology of Zhang et al.,[53] we fine-tune and distill this model into a simpler, linear graph atomic cluster expansion (GrACE) representation.[54,55] Details of the distillation framework are provided in the Supporting Information.

To fine-tune the CHGNet model, we first generate representative amorphous structures for compositions corresponding to the stable and metastable phases, namely, $BaFe_2O_4$, $Ba_2Fe_2O_5$, $BaFeO_3$, $BaFe_{12}O_{19}$, $YFeO_3$ and $Y_3Fe_5O_{12}$. This is done through a well-benchmarked workflow (MPMorph)[56,57] used extensively for the generation of amorphous structures through ab initio molecular dynamics (AIMD). We sample structures across all generated AIMD trajectories every 500 fs, and also included all structures that exhibited a cohesive energy greater than −2 eV/atom, resulting in a data set of 657 structures. This bound was determined empirically after analyzing the distributions of the MatPES r^{2}SCAN data set the foundational model is trained on, with the goal of including more high-energy states in the fine-tuning data to account for any PES softening.[58] Further, the use of AIMD was deemed necessary to avoid biasing the data set[59] toward coordination environments (and hence their implied oxidation states) that have been learned by the foundational model. We then recompute the energies, forces, stress and magnetic moments of the sampled structures through single-point DFT calculations at both the GGA-PBE and r^{2}SCAN level of theory with settings consistent with the MatPES data set[25] using the `MatPESFlowMaker` class in `atomate2`.[60]

Using the generated data, we fine-tune the foundational CHGNet using the `matgl` python package with a learning rate of 10^{-4}, which decays to 10^{-5} over 50 epochs. We applied an `energy:force:stress:magmom` weight of `1:1:0.05:1` to the loss function, which was determined through hyper-parameter tuning. All other training parameters are set to the suggested defaults. Like most semilocal equivariant models, CHGNet is not efficiently parallelizable across multiple CPUs/GPUs for molecular dynamics simulations,[55] limiting its applicability at the length and time scales required here (thousands of atoms over tens of nanoseconds). To overcome this, we perform knowledge distillation[53,61] of the fine-tuned CHGNet model into a simpler, linear graph atomic cluster expansion (GrACE) model. Despite its linear form, the FS variant of GrACE remains local and can be efficiently parallelized via domain decomposition in `LAMMPS`,[62] yielding speedups exceeding 3 orders of magnitude relative to CHGNet.[55]

For distillation, we generate training data by running 100 ps NpT molecular dynamics simulations at 1 atm using the fine-tuned CHGNet model, with the temperature ramped from 300 to 5000 K. Simulations are initialized from all Ba−Fe−Y−O structures available in the Materials Project.[11] Trajectories are sampled every picosecond, resulting in a data set of ≈20,000 structures spanning thermally perturbed crystals to liquid-like configurations. This data set is used to train the GrACE-FS potential with the `gracemaker` package, employing default training settings, loss functions, and weights. We further refine the model through a single iteration of active learning using the extrapolation-grade criterion.[63]

Downloaded from pubs.acs.org/cmatex/article-pdf/38/20/10644/6795577/acs.chemmater.6c01610.pdf by LAWRENCE BERKELEY NATL LABORATORY user on 06 November 2026

https://doi.org/10.1021/acs.chemmater.6c01610
Chem. Mater. 2026, 38, 10644−10656

Thermodynamic Hull Construction

To construct the Ba−Fe−O and Y−Fe−O interface reaction hulls, we used all entries in the Ba−Fe−Y−O chemical space from the Materials Project (v2023.11.1)[11] computed with the r^{2}SCAN functional. The $BaFe_{12}O_{19}$ phase (mp-554293) was only available at the GGA level and was therefore recomputed using r^{2}SCAN with Materials Project−compatible settings via the `MP24RelaxSet` in `pymatgen`,[64] starting from the ferromagnetic ordering.

Finite-temperature contributions were incorporated by computing heat capacities for all relevant solid phases ($BaFe_2O_4$, $Ba_2Fe_2O_5$, $BaFeO_3$, $BaFe_{12}O_{19}$, $YFeO_3$, $Y_3Fe_5O_{12}$, Fe_2O_3, Fe_3O_4, FeO, Y_2O_3, and BaO) using quasi-harmonic phonon calculations in `phonopy`[63,66] as implemented through `atomate2` with the `PhononMaker`. Energies and forces for these calculations were obtained from the fine-tuned CHGNet model, as several phases (notably $BaFe_{12}O_{19}$, $Ba_2Fe_2O_5$, and $Y_3Fe_5O_{12}$) require supercells exceeding 2000 atoms, rendering plane-wave DFT prohibitively expensive. For gaseous O_2, finite-temperature free energies were taken from the NIST−JANAF thermochemical tables.[35] For selected ferromagnetic phases with significant magnetic entropy contributions (Fe_3O_4, $BaFe_{12}O_{19}$, and $Y_3Fe_5O_{12}$), computed heat capacities were empirically corrected to match experimental data, since a rigorous treatment of the magnetic degrees of freedom (and their effect on the configurational entropy) is out of scope for this study. Finally, thermodynamic reaction networks and interface hulls were constructed using the `reaction-network` package,[5] enumerating all pairwise reactions among solid phases, with optional inclusion of gaseous species such as O_2.

Molecular Dynamics Simulations

We apply the fine-tuned CHGNet potential for density equilibration, and the trained GrACE potential to perform the production machine-learning molecular dynamics (MLMD) simulations on all experimentally observed stable crystal structure compositions in the Ba−Fe−O and Y−Fe−O hulls. The simulations were initialized using `packmol`[67] to randomly pack polyhedral units derived from Materials Project crystal structures corresponding to the target compositions. To capture the expected Fe oxidation states, we explicitly sampled coordination motifs representative of each state: octahedral $[FeO_6]$ units for Fe^{3+} and tetrahedral $[FeO_4]$ units for Fe^{2+}, extracted from the crystalline structures of Fe_2O_3 (mp-19770) and Fe_3O_4 (mp-19306), respectively.

These polyhedra are then packed together with Ba, Y, and O atoms, according to the target composition, into a cubic simulation cell containing approximately 1000 atoms. The cell dimensions are estimated from composition-dependent atomic volumes derived from Materials Project structures.[56] Starting from this randomized configuration, we perform molecular dynamics using the fine-tuned CHGNet potential, heating the system from 300 to 3000 K over 50 ps in the NPT ensemble at 1 atm using a Nose−Hoover thermostat and barostat[68] to generate an equilibrated liquid-like structure. The system is then quenched to the target temperature over an additional 50 ps (NPT), followed by 50 ps of equilibration in the NVT ensemble. After density equilibration, we switch to the distilled GrACE potential, perform a short 20 ps NVT equilibration, and then run a 20 ns production NVT simulation, collecting configurations and velocities every picosecond. The first 10% of the trajectory is discarded when extracting transport coefficients. This entire workflow is repeated three times for each composition and temperature.

Oxidation State Assignment and Polaron Mobility

To compute the screening length λ, we quantify the mobility of a small polaron M_m^e in the liquid-like phases. We use CHGNet-predicted site-wise magnetic moments on the transition-metal ions[33,69,70] to assign oxidation states, distinguishing Fe^{2+} from Fe^{3+} via a threshold on the predicted magnetic moment. The threshold is determined by a linear programming problem that enforces charge neutrality on each structure in the trajectory, with fixed oxidation states for nonmagnetic ions (Ba^{2+}, Y^{3+}, O^{2-}). For more complicated multielement systems, the Bayesian optimization approach of Barroso-Luque et al.[18] can be used instead. While a general descriptor that classifies ions into their respective oxidation state will involve features such as the coordination environments, bond lengths etc., the simpler case of Fe^{2+}/Fe^{3+} redox we consider in this work can be described through a low/high site-resolved magnetic moment. We expect this approach to directly apply for other redox couples that can be cleanly split based on the site-resolved magnetic moment, such as high-spin Mn^{3+}/Mn^{4+} or V^{4+}/V^{5+} redox couples, while splits such as Co^{2+}/Co^{3+} will require a descriptor involving more features.

A polaron hop is counted when neighboring Fe sites undergo concurrent oxidation and reduction within a 1 ps window. From the statistics of these hops we define the kinetic coefficient M_m^e and a transport coefficient L_{hop}^e analogous to the Einstein self-diffusivity of the polaron[29,71] (see Supporting Information). The resulting values of M_m^e, L_{hop}^e and λ for Fe_3O_4 and YFe_2O_4 at 1500 K are reported in the Supporting Information.

Furthermore, since time-correlation functions are destroyed when an ion undergoes "redox" and changes its identity during the simulation, we perform transport coefficient fitting in windows of one nanosecond and vary the starting frame of each window. This approach allows us to approximately recover transport differences between differently oxidized ions of the same element, since our labeling approach assigns oxidation states on a "relative" scale.[16] Recent developments in MLIPs that also perform charge equilibration[72,73] can improve this approach, but such an extension will require a mapping from abstract, MLIP-learned charges or charges partitioned from the DFT-derived charge density surface to conventional oxidation states.

Transport Coefficient Fitting

Both the self-and cross-terms of the Onsager transport matrix[74,75] are fit through the differential form of the Green−Kubo equation:

$$L_{ij} = \frac{1}{6k_B TV}\lim_{t\to\infty}\frac{d}{dt} < \Sigma_\alpha[\mathbf{r}_\alpha^i(t) - \mathbf{r}_\alpha^i(0)]\cdot\Sigma_\beta[\mathbf{r}_\beta^j(t) - \mathbf{r}_\beta^j(0)]> \tag{1}$$

wherein V and T are the volume and temperature of the system, $\mathbf{r}_\alpha^i(t) - \mathbf{r}_\alpha^i(0)$ is the displacement of the α^{th} particle of species i at time t. Readers are advised to refer to Karan et al.[12] for details on the specifics of the transport coefficient fitting.

Hence, the "specie" $i \in [Ba^{+2}, Fe^{+2}, Fe^{+3}, Y^{+3}, O^{-2}]$, depending on the expected ions in the system. We compute the "effective diffusion constant" (K_D) during a solid-state reaction through the chemical potential gradient between the reactants, given by the following expression:[12]

$$K_D = \Sigma_i\Sigma_j\frac{|L_{ij}^\gamma V^\gamma \times \min(\mu_j^\alpha - \mu_j^\beta)|}{n_i^\gamma N_A} \tag{2}$$

where V^γ is the molar volume, n_i^γ is the fraction of atoms of species i in product phase γ, N_A is the Avogadro number and μ_j^α and μ_j^β are the chemical potentials of species j in the reactants, labeled as α and β.

In the case of a mixed-valence oxide (such as Fe_3O_4), we set $\nabla\mu_{Fe^{2+}} = \nabla\mu_{Fe^{3+}}$, and fit separate transport coefficients for the 2+ and 3+ states of Fe. It is worth noting that this transport formulation yields qualitatively similar results to a model in which Fe is not partitioned into distinct oxidation states, particularly in the dilute limit. This arises because the self-term of the transport tensor in the present formulation reduces to the expression obtained when all ions of a given element are treated equivalently. To illustrate this, consider the self-part of the transport coefficient:

$$L_{ii}^{self} = \frac{1}{6k_B TV}\lim_{t\to\infty}\frac{d}{dt} < \Sigma_\alpha[\mathbf{r}_\alpha^i(t) - \mathbf{r}_\alpha^i(0)]^2>$$

$$= \frac{1}{6k_B TV}\lim_{t\to\infty}\frac{d}{dt} < \Sigma_{\alpha_i}\Sigma_{\alpha\in\alpha_i}[\mathbf{r}_\alpha^i(t) - \mathbf{r}_\alpha^i(0)]^2> \approx \Sigma_{\alpha_i}L_{\alpha_i\alpha_i}^{self}$$

The final equality holds exactly in the limit $t \to \infty$, which permits the interchange of the summation and correlation operations, and is satisfied within fitting uncertainty for MD trajectories in the diffusive

https://doi.org/10.1021/acs.chemmater.6c01610
Chem. Mater. 2026, 38, 10644−10656

Downloaded from pubs.acs.org/cmatex/article-pdf/38/20/10644/6795577/acs.chemmater.6c01610.pdf by LAWRENCE BERKELEY NATL LABORATORY user on 06 November 2026

regime. This simplification, however, does not apply rigorously to the distinct and cross terms of the transport tensor.

To quantify the deviation of transport from the dilute limit (due to distinct ion correlations), we use the correlation factor (f), which is defined as:

$$f_i = \frac{L_{ii}^{\text{dis}}}{L_{ii}^{\text{self}}} = \frac{L_{ii}}{L_{ii}^{\text{self}}} - 1 \tag{3}$$

Additionally, we analyze the local coordination environment and obtain coordination numbers for each element type within the noncrystalline phases by counting all geometrically feasible bonds for each ion within both the first and second coordination shells, which are identified through a Voronoi-based neighborhood analysis. Here both shells are included because cations typically interact through bridging O-ions. This enumeration is performed using the CrystalNN algorithm, as implemented in the `pymatgen`[64,76] python package.

ReactCA Simulations of Powder Reactions

We use a recently developed discrete cellular reaction model (ReactCA)[6] to perform powder reaction simulations. In this framework, reaction volume is discretized into voxels, where each voxel corresponds to a single particle of a specific phase. Following a combinatorial enumeration of all possible reactions at a set temperature, the simulation begins with a randomized mixture of two precursors. Over the simulation, the system iterates millions of times; at each step, it probabilistically selects reactants and converts them to products based on reaction scores (rates) and stoichiometry. Each reaction is scored using a scoring function, and we use the function proposed in Karan et al.[12] in this study, defined as:

$$S = \sigma_1\left(\frac{K_D}{r_0^2 s} \times \frac{\Delta G^*}{k_B T}\right) \times \sigma_2\left(\frac{T}{T_{m,reactant}}\right)$$

$$\sigma_1(x) = \frac{1}{3}\log(1 + \exp(ax))$$

$$\sigma_2(x) = \frac{1}{2}\log(1 + \exp(bx - c))$$

$$\Delta G^* = 1 + \text{erf}(-d(\Delta G_{rxn} + e)) \tag{4}$$

Here, K_D is the computed "effective diffusion rate constant" (eq 2), ΔG_{rxn} is the DFT computed reaction energy (finite temperature effects due to vibrational entropy are added using the heat capacity computed from quasi-harmonic phonons), T is the reaction temperature and $T_{m,\text{reactant}}$ is the melting point of the lowest-melting reactant participating in the reaction. The parameters a, b, c, d, e, r_0, and s are empirical constants obtained in Gallant et al.[6] and Karan et al.;[12] the same parameter values are used here for all reactions considered. This scoring function balances the thermodynamics and diffusion-limited factors of the reaction, while also ensuring reaction onset as per the experimental heuristic of Tammann's rule.[77] For further details about the simulation framework, readers are pointed to Gallant et al.[6]

Density Functional Theory Calculations

DFT single-point calculations and Ab-initio molecular dynamics (AIMD) calculations were performed using the Vienna Ab-Initio Simulation Package (VASP).[78,79] The Perdew−Burke−Ernzerhof (PBE) formulation of generalized gradient approximation (GGA)[80] with projector-augmented wave potentials[81,82] was used for the ab initio MD, with only the Γ-point sampled and without spin-polarization (Refer to the `MPMorphMDSet` class in `atomate2`[60] for the full input set used). All single-point calculations were done in two steps: first a GGA calculation is performed, and the computed `WAVECAR` is used as the initial guess for a meta-GGA calculation with the r^{2}SCAN functional.[83] These calculations used a plane-wave energy cutoff of 680 eV, a K-spacing of 0.2 to sample the Brillouin zone, and were spin-polarized. All settings are consistent with the `MatPESStaticSet` used in the `MatPESFlowMaker` class of `atomate2`.

■ ASSOCIATED CONTENT

Data Availability Statement

Code and Data Availability: The ReactCA simulations are performed using the `rxn-ca` Python package, and the scripts used for transport and oxidation state analysis have been made part of the `py-OATS` Python package. The transport data computed in this work are also available as part of the `rxn-ca` Python package.

Supporting Information

The Supporting Information is available free of charge at https://pubs.acs.org/doi/10.1021/acs.chemmater.6c01610.

Description of interatomic potential fine-tuning and validation; heat capacities computed with quasi-harmonic phonons and compared with experimental calorimetry; formalism for the effect of redox processes on ion transport; benchmarking of computed transport coefficients against experimental reference data (PDF)

■ AUTHOR INFORMATION

Corresponding Author

Kristin A. Persson − *Department of Materials Science and Engineering, University of California, Berkeley, California 94720, United States; Materials Sciences Division, Lawrence Berkeley National Laboratory, Berkeley, California 94720, United States;* orcid.org/0000-0003-2495-5509; Email: kapersson@lbl.gov

Author

Vir Karan − *Department of Materials Science and Engineering, University of California, Berkeley, California 94720, United States; Materials Sciences Division, Lawrence Berkeley National Laboratory, Berkeley, California 94720, United States;* orcid.org/0009-0002-2807-4389

Complete contact information is available at: https://pubs.acs.org/10.1021/acs.chemmater.6c01610

Notes

The authors declare no competing financial interest.

■ ACKNOWLEDGMENTS

This work was intellectually led by D2S2, the core program KCD2S2, which is supported by the U.S. Department of Energy, Office of Science, Office of Basic Energy Sciences, Materials Sciences and Engineering Division, under Contract No. DE-AC02-05CH11231. This research used resources of the National Energy Research Scientific Computing Center (NERSC), a U.S. Department of Energy Office of Science User Facility, operated under Contract No. DE-AC02-05CH11231. A portion of the research was performed using computational resources sponsored by the Department of Energy's Office of Energy Efficiency and Renewable Energy and located at the National Laboratory of the Rockies.

■ REFERENCES

(1) McDermott, M. J.; McBride, B. C.; Regier, C. E.; Tran, G. T.; Chen, Y.; Corrao, A. A.; Gallant, M. C.; Kamm, G. E.; Bartel, C. J.; Chapman, K. W.; et al. Assessing thermodynamic selectivity of solid-state reactions for the predictive synthesis of inorganic materials. *ACS Cent. Sci.* **2023**, *9*, 1957−1975.

Downloaded from pubs.acs.org/cmatex/article-pdf/38/20/10644/6879577/acs.chemmater.6c01610.pdf by LAWRENCE BERKELEY NATL LABORATORY user on 06 November 2026

(2) Szymanski, N. J.; Nevatia, P.; Bartel, C. J.; Zeng, Y.; Ceder, G. Autonomous and dynamic precursor selection for solid-state materials synthesis. *Nat. Commun.* **2023**, *14* (1), 6956.
(3) Szymanski, N. J.; Rendy, B.; Fei, Y.; Kumar, R. E.; He, T.; Milsted, D.; McDermott, M. J.; Gallant, M.; Cubuk, E. D.; Merchant, A.; et al. An autonomous laboratory for the accelerated synthesis of novel materials. *Nature* **2023**, *624*, 86−91.
(4) Miura, A.; Bartel, C. J.; Goto, Y.; Mizuguchi, Y.; Moriyoshi, C.; Kuroiwa, Y.; Wang, Y.; Yaguchi, T.; Shirai, M.; Nagao, M.; et al. Observing and modeling the sequential pairwise reactions that drive solid-state ceramic synthesis. *Adv. Mater.* **2021**, *33* (24), 2100312.
(5) McDermott, M. J.; Dwaraknath, S. S.; Persson, K. A. A graph-based network for predicting chemical reaction pathways in solid-state materials synthesis. *Nat. Commun.* **2021**, *12* (1), 3097.
(6) Gallant, M. C.; McDermott, M. J.; Li, B.; Persson, K. A. A Cellular Automaton Simulation for Predicting Phase Evolution in Solid-State Reactions. *Chem. Mater.* **2025**, *37*, 210−223.
(7) Chen, J.; Cross, S. R.; Miara, L. J.; Cho, J.-J.; Wang, Y.; Sun, W. Navigating phase diagram complexity to guide robotic inorganic materials synthesis. *Nat. Synth.* **2024**, *3*, 606−614.
(8) Szymanski, N. J.; Byeon, Y.-W.; Sun, Y.; Zeng, Y.; Bai, J.; Kunz, M.; Kim, D.-M.; Helms, B. A.; Bartel, C. J.; Kim, H.; et al. Quantifying the regime of thermodynamic control for solid-state reactions during ternary metal oxide synthesis. *Sci. Adv.* **2024**, *10* (27), No. eadp3309.
(9) Schmalzried, H. *Solid State Reactions*; Verlag Chemie: Weinheim, 1981.
(10) Chen, L.-Q.; Zhao, Y. From classical thermodynamics to phase-field method. *Prog. Mater. Sci.* **2022**, *124*, 100868.
(11) Horton, M. K.; Huck, P.; Yang, R. X.; Munro, J. M.; Dwaraknath, S.; Ganose, A. M.; Kingsbury, R. S.; Wen, M.; Shen, J. X.; Mathis, T. S.; et al. Accelerated data-driven materials science with the Materials Project. *Nat. Mater.* **2025**, *24*, 1522−1532.
(12) Karan, V.; Gallant, M. C.; Fei, Y.; Ceder, G.; Persson, K. A. Ion correlations explain kinetic selectivity in diffusion-limited solid-state synthesis reactions. *Nat. Mater.* **2026**, *25*, 1385−1392.
(13) Sukenaga, S.; Cicconi, M. R.; Yamada, H.; Wakihara, T.; Ohara, K.; Shibata, H.; Neuville, D. R. Iron redox effect on the structure and viscosity of a sodium silicate glass and melt. *J. Chem. Phys.* **2024**, *161* (24), 244503.
(14) Hansen, J.-P.; McDonald, I. R. In *Theory of Simple Liquids*; Fourth ed., ed.; Academic Press: Oxford, 2013; pp. 403−454.
(15) Goldman, D. S.; Gupta, P. K. Diffusion-Controlled Redox Kinetics in a Glassmelt. *J. Am. Ceram. Soc.* **1983**, *66*, 188−190.
(16) Shuaib, F.; Piotrowski, R.; Delaizir, G.; Geffroy, P.-M.; Wendji, S. D. W.; Massobrio, C.; Boero, M.; Ori, G.; Thomas, P.; Masson, O.; Bouzid, A. Quantitative assessment of the structure of (Na2O)0.1-(V2O5)0.6-(TeO2)0.3 glass: An ab initio and machine learning interatomic potential study of oxide systems with mixed-valence. *Artif. Intell. Chem.* **2026**, *4*, 100123.
(17) Neilson, J. R.; McDermott, M. J.; Persson, K. A. Modernist materials synthesis: Finding thermodynamic shortcuts with hyper-dimensional chemistry. *J. Mater. Res.* **2023**, *38*, 2885−2893.
(18) Barroso-Luque, L.; Zhong, P.; Yang, J. H.; Xie, F.; Chen, T.; Ouyang, B.; Ceder, G. Cluster expansions of multicomponent ionic materials: Formalism and methodology. *Phys. Rev. B* **2022**, *106*, 144202.
(19) Huang, G.; Montiel, D.; McAuliffe, R. D.; Veith, G. M.; Thornton, K. Phase-field modeling of solid-state metathesis reactions with the charge neutrality constraint. *Comput. Mater. Sci.* **2023**, *221*, 112080.
(20) Chen, Z.; Liu, Y.; Zhao, W.; Xiao, Y.; Li, P.; Li, J.; Zhang, P. Data-driven prediction of solid state reaction pathways in the synthesis of ferrites. *J. Solid State Chem.* **2026**, *359*, 125914.
(21) Aykol, M.; Montoya, J. H.; Hummelshøj, J. Rational Solid-State Synthesis Routes for Inorganic Materials. *J. Am. Chem. Soc.* **2021**, *143*, 9244−9259.
(22) Kohn, J. A.; Eckart, D. W.; Cook, C. F. Crystallography of the Hexagonal Ferrites. *Science* **1971**, *172*, 519−525.
(23) Van Landuyt, J.; Amelinckx, S.; Kohn, J. A.; Eckart, D. W. Multiple beam direct lattice imaging of the hexagonal ferrites. *J. Solid State Chem.* **1974**, *9*, 103−119.
(24) Deng, B.; Zhong, P.; Jun, K.; Riebesell, J.; Han, K.; Bartel, C. J.; Ceder, G. CHGNet as a pretrained universal neural network potential for charge-informed atomistic modelling. *Nat. Mach. Intell* **2023**, *5*, 1031−1041.
(25) Kaplan, A. D.; Liu, R.; Qi, J.; Ko, T. W.; Deng, B.; Riebesell, J.; Ceder, G.; Persson, K. A.; Ong, S. P.A Foundational Potential Energy Surface Dataset for Materials*arXiv***2025**
(26) Negas, T.; Roth, R. S. Synthesis of barium ferrates in oxygen. *J. Res. Natl. Bur. Stand. A Phys. Chem.* **1969**, *73A* (4), 425−430.
(27) Kitayama, K.; Sakaguchi, M.; Takahara, Y.; Endo, H.; Ueki, H. Phase equilibrium in the system Y−Fe−O at 1100 C. *J. Solid State Chem.* **2004**, *177*, 1933−1938.
(28) Bazant, M. Z. Theory of Chemical Kinetics and Charge Transfer based on Nonequilibrium Thermodynamics. *Acc. Chem. Res.* **2013**, *46*, 1144−1160.
(29) Devreese, J. T.Polarons*arXiv***2000**
(30) Austin, I.; Mott, N. Polarons in crystalline and non-crystalline materials. *Adv. Phys.* **1969**, *18*, 41−102.
(31) Helm, L.; Merbach, A. E. Inorganic and Bioinorganic Solvent Exchange Mechanisms. *Chem. Rev.* **2005**, *105*, 1923−1960.
(32) Ihle, D.; Lorenz, B. Small-polaron conduction and short-range order in Fe3 O4. *J. Phys. C: Solid State Phys.* **1986**, *19*, 5239−5251.
(33) Xie, F.; Gao, Y.; Wang, R.; Zhong, Z. Uncovering coupled ionic-polaronic dynamics and interfacial enhancement in LixFePO4. *Phys. Rev. B* **2026**, *113* (2), 024105.
(34) Mori, K.; Suzuki, K. Diffusion in Iron Oxide Melts. *Trans. Iron Steel Inst. Jpn.* **1969**, *9*, 409−412.
(35) Chase, M. *NIST-JANAF Thermochemical Tables*; 4th ed.; American Institute of Physics: Woodbury, NY, 1998.
(36) Buscaglia, V.; Caracciolo, F.; Bottino, C.; Leoni, M.; Nanni, P. Reaction diffusion in the Y2O3-Fe2O3 system. *Acta Mater.* **1997**, *45*, 1213−1224.
(37) Ingram, M. D. Ionic conductivity in glass. *Phys. Chem. Glasses* **1987**, *28*, 215−234.
(38) Holmquist, W.; Kooi, C.; Moss, R. Reaction kinetics of polycrystalline yttrium iron garnet. *J. Am. Ceram. Soc.* **1961**, *44*, 194−196.
(39) Peelamedu, R. D.; Roy, R.; Agrawal, D. K. Reaction kinetics and anisothermal effects in microwave fields: System Y2O3−Fe3O4. *J. Mater. Res.* **2001**, *16*, 2770−2772.
(40) Grosseau, P.; Bachiorrini, A.; Guilhot, B. Preparation of polycrystalline yttrium iron garnet ceramics. *Powder Technol.* **1997**, *93*, 247−251.
(41) Ali, W. F. F. W.; Othman, M.; Ain, M. F.; Abdullah, N. S.; Ahmad, Z. A. Studies on the formation of yttrium iron garnet (YIG) through stoichiometry modification prepared by conventional solid-state method. *J. Eur. Ceram. Soc.* **2013**, *33*, 1317−1324.
(42) Cortés-Escobedo, C. A.; Bolarín-Miró, A. M.; Jesús, F. S.-D.; Valenzuela, R.; Juárez-Camacho, E. P.; Samperio-Gómez, I. L.; Ammar, S.; et al. $Y_3Fe_5O_{12}$ Prepared by Mechanosynthesis from Different Iron Sources. *Adv. Mater. Phys. Chem.* **2013**, *3* (1), 41−46.
(43) Bianchini, M.; Wang, J.; Clement, R. J.; Ouyang, B.; Xiao, P.; Kitchaev, D.; Shi, T.; Zhang, Y.; Wang, Y.; Kim, H.; et al. The interplay between thermodynamics and kinetics in the solid-state synthesis of layered oxides. *Nat. Mater.* **2020**, *19*, 1088−1095.
(44) Melzer, K.; Martin, A. Moessbauer study of the reaction between barium carbonate and iron (III) oxide. *Phys. Status Solidi A* **1988**, *107*, K163−K168.
(45) Qiu, J.; Gu, M. Crystal structure and magnetic properties of barium ferrite synthesized using GSPC and HEBM. *J. Alloys Compd.* **2006**, *415*, 209−212.
(46) Shipko, M. N.; Kostishyn, V. G.; Chitanov, D. N. The Physical Model of Formation of Hexagonal Ferrites BaFe12O19. *J. Nano- Electr. Phys.* **2015**, *7*, 04046−1.

Downloaded from pubs.acs.org/cmatex/article-pdf/38/20/10644/6879577/acs.chemmater.6c01610.pdf by LAWRENCE BERKELEY NATL LABORATORY user on 06 November 2026

(47) Fujishiro, F.; Hashimoto, T. Analysis of structural phase transition from monoclinic Ba2Fe2O5 to cubic Ba2Fe2O5+ δ. *Thermochim. Acta* **2012**, *549*, 110−115.
(48) Watanabe, R.; Goto, M.; Kosugi, Y.; Kan, D.; Shimakawa, Y. Oxygen Release and Incorporation Behaviors in BaFeO3 Polymorphs with Unusually High-Valence Fe4+. *Chem. Mater.* **2024**, *36*, 2106−2112.
(49) Naveen, C.; Rohidas, A.; Raghu, S.; Havareddi, B.; Ramanna, R.; Mattyappannavar, S. *IOP Conf. Ser.: Mater. Sci. Eng.* **2024**, *1300*, 012012.
(50) Shirk, B. Ba2Fe6O11: A new metastable compound. *Mater. Res. Bull.* **1970**, *5*, 771−777.
(51) Meng, Y.; Liu, X.-W.; Huo, C.-F.; Guo, W.-P.; Cao, D.-B.; Peng, Q.; Dearden, A.; Gonze, X.; Yang, Y.; Wang, J.; Jiao, H.; Li, Y.; Wen, X.-D. When Density Functional Approximations Meet Iron Oxides. *J. Chem. Theory Comput.* **2016**, *12*, 5132−5144.
(52) Kingsbury, R.; Gupta, A. S.; Bartel, C. J.; Munro, J. M.; Dwaraknath, S.; Horton, M.; Persson, K. A. Performance comparison of r2SCAN and SCAN metaGGA density functionals for solid materials via an automated, high-throughput computational workflow. *Phys. Rev. Mater.* **2022**, *6*, 013801.
(53) Zhang, W.; Wu, X.; Wang, C.; Hu, S.; Liu, Y.; Wang, L.-W. Constructing machine learning interatomic potentials with minimum amount of ab initio data. *Npj Comput. Mater.* **2026**, *12* (1), 174.
(54) Bochkarev, A.; Lysogorskiy, Y.; Drautz, R. Graph Atomic Cluster Expansion for Semilocal Interactions beyond Equivariant Message Passing. *Phys. Rev. X* **2024**, *14*, 021036.
(55) Lysogorskiy, Y.; Bochkarev, A.; Drautz, R. Graph atomic cluster expansion for foundational machine learning interatomic potentials. *npj Comput. Mater.* **2025**, *12*, 114.
(56) Aykol, M.; Dwaraknath, S. S.; Sun, W.; Persson, K. A. Thermodynamic limit for synthesis of metastable inorganic materials. *Sci. Adv.* **2018**, *4* (4), No. eaaq0148.
(57) Zheng, H.; Sivonxay, E.; Christensen, R.; Gallant, M.; Luo, Z.; McDermott, M.; Huck, P.; Smedskjær, M. M.; Persson, K. A. The ab initio non-crystalline structure database: empowering machine learning to decode diffusivity. *Npj Comput. Mater.* **2024**, *10* (1), 295.
(58) Deng, B.; Choi, Y.; Zhong, P.; Riebesell, J.; Anand, S.; Li, Z.; Jun, K.; Persson, K. A.; Ceder, G. Systematic softening in universal machine learning interatomic potentials. *Npj Comput. Mater.* **2025**, *11* (1), 9.
(59) Bienvenu, B.; Todorova, M.; Neugebauer, J.; Raabe, D.; Mrovec, M.; Lysogorskiy, Y.; Drautz, R. Development of an atomic cluster expansion potential for iron and its oxides. *Npj Comput. Mater.* **2025**, *11* (1), 81.
(60) Ganose, A. M.; Sahasrabuddhe, H.; Asta, M.; Beck, K.; Biswas, T.; Bonkowski, A.; Bustamante, J.; Chen, X.; Chiang, Y.; Chrzan, D. C.; et al. Atomate2: Modular workflows for materials science. *Digital Discovery* **2025**, *4*, 1944−1973.
(61) Gardner, J. L. A.; du Toit, D. F. T.; Mahmoud, C. B.; Beaulieu, Z. F.; Juraskova, V.; Paşca, L.-B.; Rosset, L. A. M.; Duarte, F.; Martelli, F.; Pickard, C. J.; Deringer, V. L.Distillation of atomistic foundation models across architectures and chemical domains*arXiv* **2025**
(62) Thompson, A. P.; Aktulga, H. M.; Berger, R.; Bolintineanu, D. S.; Brown, W. M.; Crozier, P. S.; In't Veld, P. J.; Kohlmeyer, A.; Moore, S. G.; Nguyen, T. D.; Shan, R.; Stevens, M. J.; Tranchida, J.; Trott, C.; Plimpton, S. J. LAMMPS - a flexible simulation tool for particle-based materials modeling at the atomic, meso, and continuum scales. *Comput. Phys. Commun.* **2022**, *271*, 108171.
(63) Lysogorskiy, Y.; Bochkarev, A.; Mrovec, M.; Drautz, R. Active learning strategies for atomic cluster expansion models. *Phys. Rev. Mater.* **2023**, *7*, 043801.
(64) Ong, S. P.; Richards, W. D.; Jain, A.; Hautier, G.; Kocher, M.; Cholia, S.; Gunter, D.; Chevrier, V. L.; Persson, K. A.; Ceder, G. Python Materials Genomics (pymatgen): A robust, open-source python library for materials analysis. *Comput. Mater. Sci.* **2013**, *68*, 314−319.
(65) Togo, A.; Chaput, L.; Tadano, T.; Tanaka, I. Implementation strategies in phonopy and phono3py. *J. Phys.: Condens. Matter* **2023**, *35*, 353001.
(66) Togo, A. First-principles Phonon Calculations with Phonopy and Phono3py. *J. Phys. Soc. Jpn.* **2023**, *92*, 012001.
(67) Martínez, L.; Andrade, R.; Birgin, E. G.; Martínez, J. M. PACKMOL: A package for building initial configurations for molecular dynamics simulations. *J. Comput. Chem.* **2009**, *30*, 2157−2164.
(68) Evans, D. J.; Holian, B. L. The Nosé−Hoover thermostat. *J. Chem. Phys.* **1985**, *83*, 4069−4074.
(69) Zhong, P.; Deng, B.; Anand, S.; Mishra, T.; Ceder, G. Modeling phase transformations in Mn-rich disordered rocksalt cathodes with machine-learning interatomic potentials. *Phys. Rev. Mater.* **2025**, *9* (10), 105404.
(70) Birschitzky, V. C.; Leoni, L.; Reticcioli, M.; Franchini, C. Machine Learning Small Polaron Dynamics. *Phys. Rev. Lett.* **2025**, *134*, 216301.
(71) Baranovskii, S.; Faber, T.; Hensel, F.; Thomas, P. On the Einstein relation for hopping electrons. *J. Non-Cryst. Solids* **1998**, *227−230*, 158−161.
(72) Fuchs, P.; Sanocki, M.; Zavadlav, J. Learning non-local molecular interactions via equivariant local representations and charge equilibration. *Npj Comput. Mater.* **2025**, *11* (1), 287.
(73) Ko, T. W.; Liu, R.; Mishra, A. R.; Yu, Z.; Qi, J.; Ong, S. P. A.Fast, Accurate, and Reactive Equivariant Foundation Potential*arXiv* **2025**
(74) Fong, K. D.; Self, J.; McCloskey, B. D.; Persson, K. A. Onsager transport coefficients and transference numbers in polyelectrolyte solutions and polymerized ionic liquids. *Macromolecules* **2020**, *53*, 9503−9512.
(75) Fong, K. D.; Bergstrom, H. K.; McCloskey, B. D.; Mandadapu, K. K. Transport phenomena in electrolyte solutions: Nonequilibrium thermodynamics and statistical mechanics. *AIChE J.* **2020**, *66* (12), No. e17091.
(76) Zimmermann, N. E.; Jain, A. Local structure order parameters and site fingerprints for quantification of coordination environment and crystal structure similarity. *RSC Adv.* **2020**, *10*, 6063−6081.
(77) Merkle, R.; Maier, J. On the tammann−rule. *Z. für Anorg. Allg. Chem.* **2005**, *631*, 1163−1166.
(78) Kresse, G.; Furthmüller, J. Efficient iterative schemes for *ab initio* total-energy calculations using a plane-wave basis set. *Phys. Rev. B* **1996**, *54*, 11169−11186.
(79) Kresse, G.; Furthmüller, J. Efficiency of ab-initio total energy calculations for metals and semiconductors using a plane-wave basis set. *Comput. Mater. Sci.* **1996**, *6*, 15−50.
(80) Perdew, J. P.; Burke, K.; Ernzerhof, M. Generalized Gradient Approximation Made Simple. *Phys. Rev. Lett.* **1996**, *77*, 3865−3868.
(81) Blöchl, P. E. Projector augmented-wave method. *Phys. Rev. B* **1994**, *50*, 17953−17979.
(82) Kresse, G.; Joubert, D. From ultrasoft pseudopotentials to the projector augmented-wave method. *Phys. Rev. B* **1999**, *59*, 1758−1775.
(83) Furness, J. W.; Kaplan, A. D.; Ning, J.; Perdew, J. P.; Sun, J. Accurate and Numerically Efficient r2SCAN Meta-Generalized Gradient Approximation. *J. Phys. Chem. Lett.* **2020**, *11*, 8208−8215.

Downloaded from pubs.acs.org/cmatex/article-pdf/38/20/10644/6879577/acs.chemmater.6c01610.pdf by LAWRENCE BERKELEY NATL LABORATORY user on 06 November 2026